A 3-D Ultrasound-Based Framework to Characterize the Echo Morphology of Carotid Plaques

José C. R. Seabra*, *Student Member, IEEE*, Luís M. Pedro, José Fernandes e Fernandes, and João M. Sanches, *Member, IEEE*

***Abstract*—Carotid atherosclerosis is the main cause of brain stroke, which is the most common life-threatening neurological disease. Nearly all methods aiming at assessing the risk of plaque rupture are based on its characterization from 2-D ultrasound images, which depends on plaque geometry, degree of stenosis, and echo morphology (intensity and texture). The computation of these indicators is, however, usually affected by inaccuracy and subjectivity associated with data acquisition and operator-dependent image selection. To circumvent these limitations, a novel and simple method based on 3-D freehand ultrasound is proposed that does not require any expensive equipment except the common scanner. This method comprises the 3-D reconstruction of carotids and plaques to provide clinically meaningful parameters not available in 2-D ultrasound imaging, namely diagnostic views not usually accessible via conventional techniques and local 3-D characterization of plaque echo morphology. The labeling procedure, based on graph cuts, allows us to identify, locate, and quantify potentially vulnerable foci within the plaque. Validation of the characterization method was made with synthetic data. Results of plaque characterization with real data are encouraging and consistent with the results from conventional methods and after inspection of surgically removed plaques.**

***Index Terms*—Carotid atherosclerosis, labeling with graph cuts, plaque echo morphology, reconstruction, three-dimensional ultrasound.**

I. Introduction

In WESTERN countries, atherosclerosis is the most prevalent and main cause of death and disability in adults. It is a disease of the large- and medium-sized arteries, and its most important feature is plaque formation owing to progressive subendothelial accumulation of lipid, protein, and cholesterol esters in the blood vessel wall.

The degree of stenosis[1] is targeted as one of the most important physiological landmarks of stroke risk, and it was, until recently, the main criterion used to decide about surgical intervention [1], together with age, health, and patient's clinical history. The benefit of endarterectomy is clearly demonstrated for patients presenting high degree of stenosis (more than 60%) [2]. It has also been shown, however, that patients on medical treatment remained free of symptoms for a long period despite the presence of considerable stenotic lesions. This suggests that the degree of stenosis alone is not enough for assessment of plaque risk and that other factors should be taken into account [3].

A significant effort is being made in the study of accurate and reproducible techniques, and indicators to monitor plaque progression and risk, namely by use of ultrasound, intravenous digital subtraction angiography (IV-DSA), MRI, and computed tomographic angiography (CTA) or 3-D-CTA. Ultrasound is noninvasive, does not involve ionizing radiation, gives results in real time, and is less expensive than other imaging modalities, whereas its major limitations are the poor soft tissue contrast compared with MRI or CT and high operator dependency. The framework described in this paper is based on ultrasound, and therefore, it is not expected to outperform other state-of-the-art methods based on MRI or CT in terms of accuracy. The goal is to provide significant improvements on the traditional and widely performed diagnostic method based on freehand 2-D ultrasound without compromising the technological simplicity, nonexpenditure, and accessibility of this diagnostic procedure.

Plaque morphology is currently considered relevant for evaluation of stroke risk in carotid atherosclerosis [3]. The most important parameters to characterize the plaque are its morphology, echogenicity,[2] and texture. Several studies have statistically characterized the morphology and texture of carotid plaques in 2-D ultrasound images using a stratified GSM analysis and color mapping of the plaque [4]. The GSM is used to classify plaques as hypoechogenic (GSM $<$ 32) or hyperechogenic (GSM $>$ 32) [3], [5]. The total percentage of hypoechogenic pixels (P_{40}, also known as PEP), defined as the percentage of pixels with gray levels below 40, is also an important measure for the characterization of plaque echogenicity [3]. Multiple regression analysis has revealed that the GSM and the P_{40} are the most significant variables related to the presence of disease symptoms. Recently, an activity index [5] was proposed by one of the authors, which can be defined as a quantitative index resulting from a weighted sum of scores ascribed to the degree of stenosis, global GSM and P_{40}, and location of hypoechogenic sites across the plaque. This measure may have relevant clinical significance in therapeutic decision in patients with asymptomatic carotid lesions or with symptomatic stenosis with moderate obstruction.

A vulnerable plaque is associated with thinning of the fibrous cap and infiltration of inflammatory cells, consequently leading

Manuscript received May 20, 2008; revised November 14, 2008. First published February 6, 2009; current version published May 22, 2009. This work was supported by the Fundação para a Ciência e Tecnologia under the Institute for Systems and Robotics/Instituto Superior Técnico (ISR/IST) pluriannual funding. *Asterisk indicates corresponding author.*

*J. C. R. Seabra is with the Institute for Systems and Robotics, Instituto Superior Técnico, Lisbon 1049-001, Portugal (e-mail: jseabra@isr.ist.utl.pt).

L. M. Pedro and J. Fernandes e Fernandes are with the Cardiovascular Institute and the Lisbon University Medical School, Hospital de Santa Maria, Lisbon 1600-190, Portugal.

J. M. Sanches is with the Institute for Systems and Robotics, Instituto Superior Técnico, Lisbon 1049-001, Portugal (e-mail: jmrs@ist.utl.pt).

Color versions of one or more of the figures in this paper are available online at http://ieeexplore.ieee.org.

Digital Object Identifier 10.1109/TBME.2009.2013964

[1]Narrowing of the arterial lumen.

[2]Degree to which sound waves are reflected by a tissue.

to plaque rupture. Studies that correlate quantitative analysis based on ultrasound B-mode images with histology have suggested that hypoechogenic regions have more fatty contents and hemorrhage, indicating inflammatory activity and potential instability [6]. Therefore, the location and extension of these regions within the plaque could be a sensitive and relevant marker of stroke risk. Analysis of global information about plaque morphology may not be accurate enough in many cases, namely when plaques are heterogeneous or present significant hypoechogenic regions. An averaged measure of echogenicity or texture is incomplete and does not reveal possible unstable foci inside the plaque.

The risk assessment of plaque rupture through conventional 2-D techniques is limited to a subjective selection of a representative image of plaque structure and it is not reproducible. An accurate diagnostic methodology based on 3-D is known to be valuable but has not yet been adopted in clinical practice, mainly because 3-D ultrasound technology is not usually available in most medical facilities. Recently, less operator-dependent methods based on 3-D ultrasound have been proposed for better assessment of plaque vulnerability [7]. These studies aim at quantifying the plaque volume, the degree of stenosis [8], and the level of surface ulceration [9].

The common carotids are the major arteries that supply the brain and face tissues with blood. They are located on each side of the neck along its longitudinal axis. Each one branches off in external and internal carotids, behind the mandibular angle, along the upward direction. The most frequent location of the atherosclerotic lesion in the cerebrovascular sector is the carotid bifurcation and in the junction between common and internal carotids. Here, plaque formation tends to produce stenosis, reducing the blood flow or, even worse, causing liberation of thrombi that embolize downstream. The focus of this paper is on the 3-D reconstruction of bifurcation plaques in order to characterize their echo morphology and to evaluate their risk of rupture. In this paper, three important novelties are introduced: 1) a simple acquisition protocol for plaque reconstruction that does not need any additional equipment, such as spatial locators or mechanical sweepers but only the common scanner; 2) a set of new indicators of plaque echo morphology computed on a 3-D basis; 3) a voxelwise characterization method where potentially vulnerable foci inside the plaque are labeled and identified.

This paper is organized as follows. Section II formulates the problem and describes the acquisition protocol. Section III describes the reconstruction method, including segmentation and reconstruction. Section IV refers to plaque characterization and Section V presents the experimental results. Section VI concludes the paper.

II. Materials and Methods

In 3-D ultrasound, a sequence of images corresponding to different positions and orientations of the probe is used to extract anatomical details such as organ boundaries or contents of a volume of interest (VOI) [7]. The simple geometry of the carotid and its superficial location make it possible to acquire a set of images corresponding to nearly parallel cross sections of the bifurcation without using any kind of spatial locators. The acquisition protocol is critical to guarantee the quality of results. Because no spatial locators are being used, this process must be carefully handled since the true positions and orientations of the planes are not accurately known. A PC-camera-based application is provided to the medical doctor to help in monitoring the velocity of the ultrasound probe during a preacquisition training stage. This information is used to improve the application of the protocol that requires a constant orientation of the probe and a nearly constant linear velocity along the carotid main axis during image acquisition (see Appendix A).

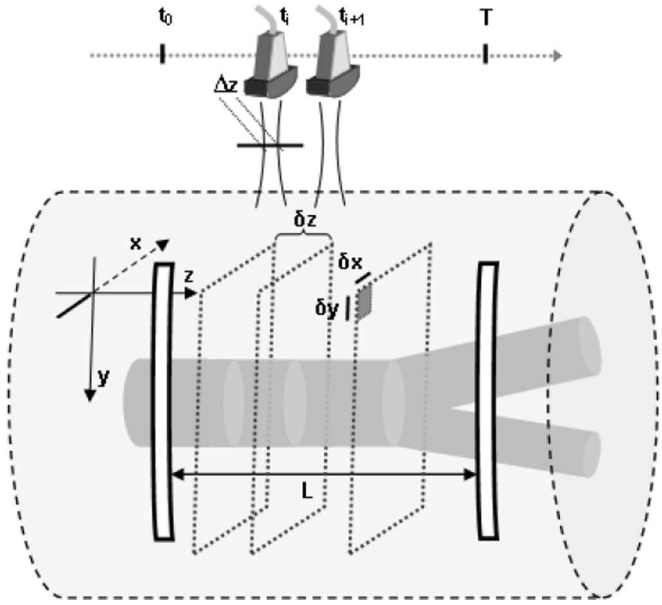

Fig. 1. Acquisition protocol. The ultrasound probe is placed transversally to the neck and an image sequence is recorded by sweeping it over a known path limited by specific landmarks.

Five carotid arteries were part of this study, one acquired from a healthy person (hereafter called JS1N06) and the others from asymptomatic patients (hereafter called FC2A06, CN1A07, JF1A08, and JB1A08), obtained during routine medical examinations. All these were examined on a standard, commercial ultrasound duplex scanner (HDI 5000, Philips Medical Systems Division, Bothell, WA) using an L12-5 scan probe (5–12 MHz broadband linear array transducer), operating in B-mode. In a typical acquisition session, 60 images (768×576 pixels) are acquired during a period of 4 s and then stored in the scanner frame buffer (cineloop). The acquisition procedure is illustrated in Fig. 1, where the strips, separated by a known distance, are rigorously placed in the patient's neck to work as landmarks for signaling the limits of the probe path.

The uncertainty about the true position and orientation of the probe introduces geometric distortions that degrade the results. A realistic theoretical model (see Appendix A) was derived to describe the probe displacement and the theoretical errors were also derived along the whole probe course. The comparison of these theoretical errors with the experimental ones has shown the adequacy of the model. This theoretical analysis is important for choosing the optimal parameters to be used in a given

TABLE I
GLOBAL CHARACTERIZATION OF CAROTID PLAQUES: DIAGNOSTIC PARAMETERS OBTAINED WITH 2-D METHODS (AREA A, LONGITUDINAL EXTENSION ℓ, MEAN μ, MEDIAN υ, STANDARD DEVIATION σ, AND $P40$) AND WITH 3-D METHOD (VOLUME V, LONGITUDINAL EXTENSION ℓ, AVERAGED VALUES OF $\hat{f}_\tau$, WHERE $\tau = \mu, \upsilon, \sigma,$ AND P_{40})

2D conventional method												**3D method**
Patients	A(mm^2)		V(mm^3)	$\ell\ (mm)$		μ_{y_o}	$\overline{\hat{f}}_\mu$	υ_{y_o}	$\overline{\hat{f}}_\upsilon$	σ_{y_o}	$\overline{\hat{f}}_\sigma$	$P40_{y_o}$ $\overline{\hat{f}}_{P_{40}}$
CN1A07	69	**1058**	24.33	**22.66**	44.00	**48.04**	40	**45**	27.83	**25.11**	50.62	**55.32**
JF1A08	73	**2201**	43.70	**44.10**	29.50	**37.34**	28	**35**	18.50	**20.12**	76.83	**71.82**
FC2A06	70	**1911**	39.13	**42.50**	30.76	**29.10**	24	**27**	25.41	**21.43**	59.83	**57.59**
JB1A08	32	**508**	38.75	**39.99**	24.50	**23.29**	22	**22**	19.03	**18.17**	61.65	**63.26**

experiment: number of images, length of the course, frame rate, and maximum position error expected. In order to evaluate the magnitude of the acquisition errors, 50 tests using a spatial locator were carried out. These tests show that it is possible for a trained operator to acquire images with small position errors and orientation angle variations. These errors are even more attenuated after alignment is performed in the data processing stage.

The data structure used in the reconstruction step is as follows: the interplane distance is given by $\delta_z = L/(N-1)$, where L is the known total length of the sweep path, limited by specific landmarks made of ultrasound echo absorption material (see Fig. 1), and the position of each pixel is computed as $x^p_{i,j} = (i\delta_x, j\delta_y, p\delta_z)$, where p is the image index. δ_x and δ_y are the interpixel distances that are constant for all images and given by the scanner. δ_x and δ_y depend on the image resolution and δ_z is estimated along the sweep path. For a 768×576 pixel image size, $L = 80 \pm 0.5$ mm course length and $N = 60$ images, $\delta_x = \delta_y = 6.1 \times 10^{-3}$ cm and $\delta_z = 1.3 \times 10^{-1}$ cm.

Ultrasound images present a low SNR and are corrupted by a particular type of multiplicative noise called speckle. Commercial ecographs perform nonlinear image compression to reduce the dynamic range of the RF signal in order to improve image visualization. Moreover, the clinician may adjust other parameters, such as brightness, gain, and contrast. These operations significantly change the statistical distribution of the original RF raw data, which is assumed in a wide range of situations to be Rayleigh-distributed [10].

Under the assumption of fully developed speckle, the compressed ultrasound image is described by a Fisher–Tippett distribution [11]. The fully developed speckle arises when the number of scatters per resolution cell is large, the echo complex magnitude components in phase and quadrature are normally distributed, and the complex phase is uniformly distributed. Deviations from this model occur when strong specular reflections associated with transitions are present in the images. In these cases, other distributions should be used to describe the observed data [12], [13]. Here, the fully developed speckle is not insured; however, the comparison of the indicators shown in Table I suggests that this assumption is acceptable for the purpose of plaque characterization.

III. RECONSTRUCTION

Two approaches are generally considered in organ and tissue reconstruction: surface and volume rendering. In this paper, a surface rendering approach is used to reconstruct the bifurcation walls and quantify the degree of stenosis and plaque volume. A volume rendering approach is used to reconstruct the VOI containing the plaque in order to perform its characterization. Statistical measures derived from the reconstructed plaque are then used to detect within the plaque unstable regions with potential risk of rupture.

A. Modeling Log-Compressed Ultrasound Data

In this paper, an algorithm for the log-compressed observed dataset (image) [14] was used to estimate the RF signal provided by the ultrasound probe. It is important that the processing operations inherent in the acquisition equipment and settings could be reverted in order to obtain estimates of the original Rayleigh-distributed data. This step is crucial to guarantee objective, realistic, and reproducible models for data reconstruction and characterization.

The preprocessing procedure performed by the ultrasound equipment is modeled as follows:

$$z_{ij} = \alpha \log(y_{ij} + 1) + \beta \tag{1}$$

where the $\log$ function accounts for the compression, (α, β) are unknown parameters that account for the contrast and brightness, respectively, and z_{ij} is the intensity at the (i, j)th observed pixel. These parameters can be estimated directly from the observed images [14] as follows:

$$\hat{\alpha} = \sqrt{\frac{24}{\pi^2}\,\sigma_z^2} \tag{2}$$

and

$$\hat{\beta} = \mu_z - \frac{\hat{\alpha}}{2}\left(\log(2\hat{\psi}) - \gamma\right) \tag{3}$$

where $\gamma = 0.5772\ldots$ is the Euler–Mascheroni constant and ψ can be obtained by the Newton–Raphson method $\psi^{t+1} = \psi^t - F(\psi)/F'(\psi)$, with $F(\psi) = (\alpha/2)\log(2\,\psi) - (\alpha\gamma/2) - \alpha A(\psi) - \mu_z + \min(z) = 0$. By incorporation of the estimates of α and β in (1) and inverse transformation of (1), the original Rayleigh-distributed data y are recovered and used hereafter.

B. Segmentation of Carotid and Plaque Boundaries

Segmentation of carotid and plaque boundaries is performed with a feature-based approach [7] on an image-by-image basis, where contours of both structures are extracted from each image of the sequence. Other strategies may be used, such as active surfaces [15] or level sets [16]. This strategy was adopted, however, because it favors interaction with the clinician who is familiar with the traditional 2-D ultrasound analysis. In fact, the proposed algorithm is semiautomatic in the sense that the clinician may intervene with the process every time he/she judges the automatic segmentation is taking wrong decisions. The surface meshes of the carotid and plaque are obtained by linking of the contours. Extraction of carotid and plaque boundaries is performed in five steps, which are listed and briefly described as follows.

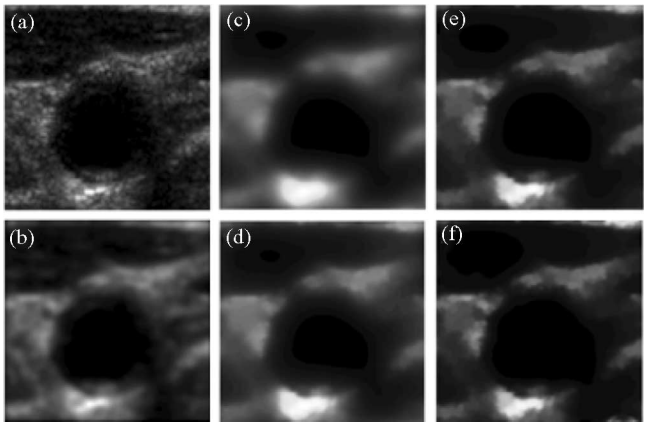

Fig. 2. Denoising methods. (a) Original (noisy) and denoised images using median and Gaussian filters. (b) Method based on the MAP criterion with a TV edge-preserving prior at iterations (c) 1, (d) 5, (e) 15, and (f) 20.

1) Denoising: Several techniques have been proposed for denoising ultrasound images without distorting the relevant clinical details [17], [18]. Bayesian methods have been successfully used in several medical imaging modalities [19]. These algorithms, however, are time-consuming and computationally demanding.

In this paper, a denoising algorithm described in [20] is used. The algorithm uses the *maximum a posteriori* (MAP) criterion with a *total variation* (TV) edge-preserving *Gibbs* prior. The method is formulated as an optimization task that is solved by the Sylvester equation [20]. In order to speedup the processing time of the sequence, the initialization of the iterative filter at each image is performed by use of the previous denoised image in the sequence. Fig. 2 displays an example of denoising results of a 280×280 pixel noisy image [Fig. 2(a)] using two methods: 1) a common despeckling filter consisting of a combination of a 10×10 window median filter with a $\sigma = 3$ Gaussian filter [Fig. 2(b)]; and 2) the MAP filter [Fig. 2(c)–(f)] at different stages of the process. Denoising results using the MAP method clearly show a better preservation of the clinically relevant anatomic details, which is thereafter useful for segmentation.

2) Extraction of Boundaries With 2-D Active Contours: The 2-D *gradient vector flow*- (GVF) active contours algorithm [21] is used to automatically segment the anatomic objects present in the denoised images. An exception is made in the first image of the sequence where the clinician must manually define the centers of the carotids [Fig. 3(a)]. Under normal conditions, the initial contour used by the GVF algorithm in a given cross section is obtained from the segmentation of the previous image, as displayed in Fig. 3(b). The clinician, however, may intervene with the process by changing the initial contour or the default parameters used by the algorithm. This functionality is useful when the GVF algorithm converges to a wrong contour due to bad initialization or when topological modifications arise. Two important situations need a special consideration: 1) the bifurcation plane, where the two contours coming from the plane above converge and merge into a single one, after removal of the intersecting region [Fig. 3(c)–(f)]. The new single contour is used as initialization to segment the carotid in the bifurcation cross section [Fig. 3(f)]. 2) the first image where the plaque is visually detected [Fig. 3(g) and (h)]. Because the plaque is a complex structure, the clinician must manually initialize its contour, whereas the other images containing the plaque are semiautomatically segmented. The ability to control the automatic procedure in each step is useful, namely for

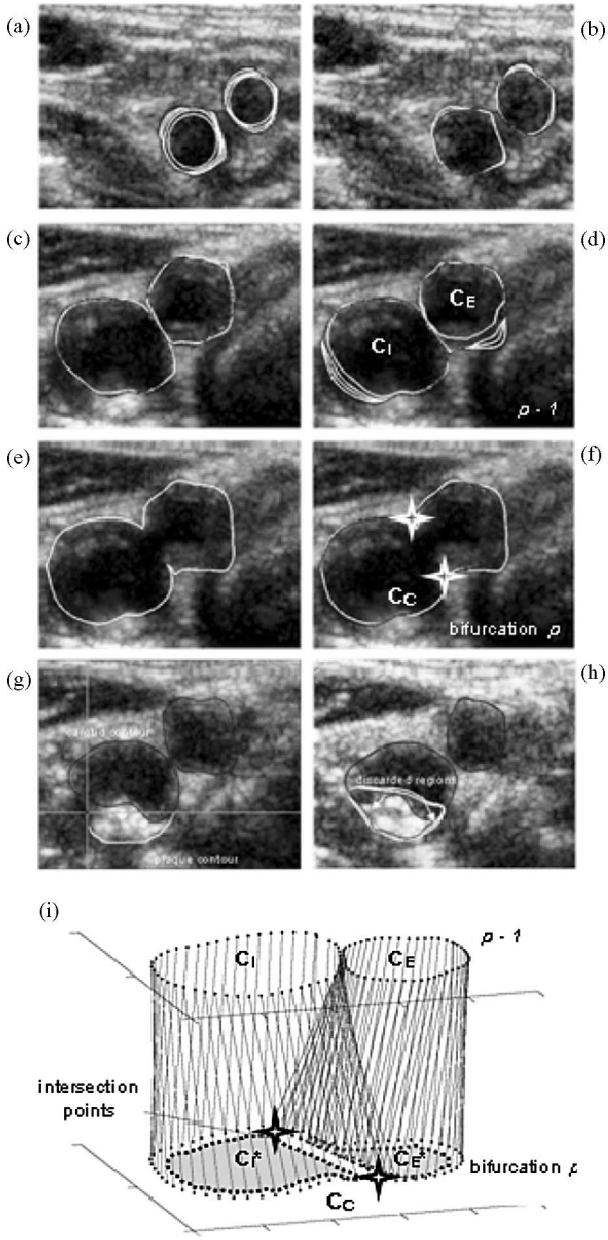

Fig. 3. Segmentation results superimposed with the original images. (a) Initialization of the active contours. (b) In the following cross section, contours from the previous segmentation (black) are used as initial estimations leading to new contours (white). (c)–(f) Segmentation of the carotid artery at the bifurcation. (g) and (h) Manual outlining in the first image where the plaque is visually detected. The active contours algorithm produces close contours for both the carotid and plaque, which are thereafter reconciled, preserving the carotid contour and trimming the plaque contour. (i) Bifurcation linking. The contours C_I and C_E derived from the previous plane merge in the bifurcation plane p, creating two intersection points that are linked to define a "virtual line." Both contours are then reconciled with this virtual line, creating, after resampling, two "virtual" contours $C_I{}^*$ and $C_E{}^*$. These are then matched to the contours in the plane $p-1$.

detecting plaque contours, because they may present a complex morphology [Fig. 3(g) and (h)]. This complexity may lead to segmentation errors in a completely automatic algorithm; thus, a semiautomatic procedure is more suitable. In about 10% of the images, it is necessary to interfere in the segmentation process and change the 2-D active contour parameters or initialization.

3) Resampling and Linking: The surface meshes representing the carotid and plaque are obtained by linking of the several contours derived from the segmentation procedure. These contours, described by a set of unevenly spaced control points, are orderly and evenly resampled, thus allowing us to match contours in consecutive planes.

The linking procedure establishes a pairing relation between homologous control points in two consecutive contours. This task is performed by use of the iterative closest point (ICP) algorithm [22]. In this method, rotation and translation transformations are estimated to minimize the overall distance between both sets of points. This strategy is repeated for each pair of contours. The pairing process at the bifurcation requires a special consideration because there is a relevant topological change. As shown in Fig. 3(i), two additional contours, C_I* and C_E*, are created in the bifurcation plane to link the two contours C_I and C_E, respectively, from the plane above.

4) Alignment: In order to compensate for small lateral probe displacements during acquisition, an alignment procedure of the contours along the longitudinal direction is needed. The alignment is performed on a pairwise basis, where each pair of two consecutive contours is aligned one at a time.

This is done by minimizing an energy function involving translation vectors associated with each image. In order to obtain smooth surfaces, a regularization parameter is used. The energy function to be minimized is

$$E_i = \sum_{k=0}^{L-1} \left[p_i(k) - p_{i-1}(k) - t_i\right]^2 + \alpha\, \Delta t_i^2 \qquad (4)$$

where $p_i(k)$ is the kth control point of the ith contour, t_i is the misalignment compensation translation vector associated with the ith image, $\Delta t_i = t_i - t_{i-1}$ are the differences between consecutive vectors, and α is the regularization parameter. The use of matrix notation leads to $E_i = (P_i - P_{i-1} - \theta t_i)^T (P_i - P_{i-1} - \theta t_i) + \alpha (t_i - t_{i-1})^T (t_i - t_{i-1})$, where $P_i = [p_{ix}(0), p_{iy}(0), \ldots, p_{ix}(L-1), p_{iy}(L-1)]^T$, $t_i = [t_{ix}, t_{iy}]^T$, and

$$\theta = \begin{pmatrix} 1 & 0 & 1 & \cdots & 0 & 1 \\ 0 & 1 & 0 & \cdots & 1 & 0 \end{pmatrix}^T.$$

The vector that minimizes (4) is $t_i = (\theta^T\theta + \alpha I)^{-1}[\theta^T (P_i - P_{i-1}) + \alpha t_{i-1}]$.

The alignment result is shown in Fig. 4(a), where estimated translation vectors are added to the positions of control points for each plane. Fig. 4(c) shows the smoothed curve fitted to the estimated translation vector components, representing its space-varying mean. These smoothed curves are subtracted from the estimated translation vector components to avoid alignment compensation of real anatomical deviations between planes, not originated during the acquisition process. Fig. 4(b) displays the correct alignment of the contours with this mean compensation.

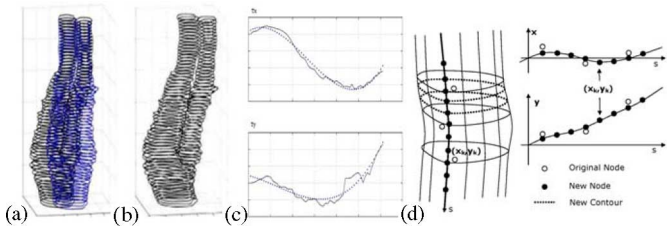

Fig. 4. (a) Absolute alignment (gray) of original contours (black). (b) Corrected alignment using dynamic mean. (c) Translation vectors components in x and y (line) and smoothed version (dots). (d) Longitudinal interpolation and smoothing.

5) Generation of Surface Meshes: In a final step, the linked contours are interpolated and smoothed along the longitudinal axis, as shown in Fig. 4(d). The goal is to increase the resolution of the initial mesh and smooth its surface by creating new contours from the ones obtained during the segmentation step. Here, interpolation is performed along a longitudinal line, as shown in Fig. 4(d).

C. Plaque Reconstruction

Plaque reconstruction is performed from the noisy pixel observations extracted from its interior after log-compression compensation. The reconstruction is performed in a Bayesian framework, where the observations have Rayleigh statistics and a TV-based Gibbs distribution is used to regularize the solution. This prior distribution is suitable to fill the interplane gaps if they exist and interpolate the observed data to attenuate the speckle noise and the discontinuities that arise during image acquisition. It must, however, be insured that a maximum sweeping speed is not exceeded to avoid undersampling situations. This is not difficult to achieve since the geometry to be reconstructed is topologically simple. Therefore, the minimum number of images needed to avoid undersampling is $N_{\min} = L/\Delta_z$, where L is the total length of the course and Δ_z is the length of the point spread function (PSF) in the z-direction, orthogonal to the plane XY of the image (see Fig. 1). In this paper, $N_{\min} \approx 100$ is shown to be adequate for $L = 10$ cm, which means ten images per centimeter. For a frame rate $F_s = 25$ images per second, this image density may be obtained with an acquisition time $T \approx 4$ s. In fact, the image density used is higher: for $L = 8$ cm and $T = 4$ s, the image density is $T \cdot F_s/L = 12.5$ images per centimeter.

The plaque inner region is modeled as a continuous function expressed as a linear combination of basis functions

$$f(x) = \sum f_k \phi_k(x) \qquad (5)$$

where $\phi_k(x)$ are finite-support trilinear interpolating basis functions. These functions are located at the nodes of a 3-D regular grid with which the f_k coefficients to be estimated are associated. Pixels observed inside the plaque are corrupted by speckle noise. The estimation of $f(x)$ is performed in a Bayesian framework where the observation model for the compensated

RF-estimated data y (Section III-A) is described by a Rayleigh distribution given by

$$p(y|f) = \frac{y}{f(x)} e^{-y^2/2f(x)} \tag{6}$$

and the prior function is the following:

$$p(F) = \frac{1}{Z} e^{-\alpha\,\mathrm{TV}} \tag{7}$$

where Z is a partition function and α is a parameter used to tune the smoothness of the solution. TV is $\sum g_k$, where g_k is the gradient magnitude of $f(x)$, $|\nabla f(x)|$, computed at the kth node. This gradient magnitude can be approximated as $g_k = \sqrt{\sum_{j=1}^{6} (f_k - f_{k_j})^2}$, where f_{k_j} are the six neighbors of f_k.

The estimation problem used in this paper is based on the method described in [23]. In this method, the reconstruction—by using the MAP criterion—is formulated as the following optimization task where an energy function is minimized:

$$\hat{F} = \arg\min_{F} E(Y, X, F). \tag{8}$$

$F = [f_1, f_2, \ldots, f_N]^T$ is a vector of coefficients, defining $f(x)$ [see (5)], to be estimated from a set of observations $Y = \{y_i\}$ and corresponding positions $X = \{x_i\}$. The energy function is composed of two terms

$$E(Y, X, F) = E_Y(Y, X, F) + E_F(F) \tag{9}$$

where $E_Y(Y, X, F)$ and $E_F(F)$ are called *data fidelity term* and *prior term*, respectively. The minimization of (9) is done by finding its stationary point, i.e., $\nabla E(Y, X, F) = 0$ [23]. Using a Gauss–Seidel approach, the minimization of $E(Y, X, F)$ is performed by keeping all unknowns constant, but one at a time. Each resulting unidimensional equation is solved by the Newton–Raphson method. The overall solution is obtained by solving the following set of equations:

$$\frac{\partial E_Y(Y, X, F)}{\partial f_k} + \frac{\partial E_F(F)}{\partial f_k} = 0 \tag{10}$$

for $0 \le k \le N-1$, where N is the number of coefficients to be estimated. This leads to

$$\frac{\partial E(Y, X, F)}{\partial f_k} = \frac{1}{2} \sum \frac{2f(x_i) - y_i^2}{f^2(x_i)} \phi_k(x_i) + \frac{6\alpha}{g_k}[f_k - \overline{f_k}] = 0 \tag{11}$$

where $\overline{f_k} = (1/N_V) \sum_\tau f_{k\tau}$ is the average intensity of the neighbors of f_k, $f_{k\tau}$ is the τth neighbor of f_k, N_v is the number of neighbors of f_k, and g_k is the gradient magnitude at the kth node. Approximating $f(x_i) \approx f_k$ leads to

$$\frac{1}{f_k} \sum \phi_k x_i - \frac{1}{2f_k^2} \sum y_i^2 \phi_k(x_i) + \frac{6\alpha}{g_k}(f_k - \overline{f_k}) = 0. \tag{12}$$

The solution of this equation with the Newton–Raphson method results in the following recursion:

$$f_k^{t+1} = f_k \frac{6\alpha \overline{f}_k f_k^2 - 2 f_k b_k g_k + 3 f_k^{\mathrm{ML}} g_k}{6\alpha \overline{f}_k f_k^3 - b_k f_k g_k + 2 f_k^{\mathrm{ML}} g_k}. \tag{13}$$

The initialization is performed with a *maximum likelihood* (ML) estimation $F^{\mathrm{ML}} = [f_k^{\mathrm{ML}}]^T$

$$f_k^{\mathrm{ML}} = \frac{\sum_{i \in V(k)} y_i^2 \phi_k(x_i)}{\sum_i \phi_k(x_i)} \tag{14}$$

where $V(k)$ is the set of indexes of the observations located in the support region of $\phi_k(x)$. Note that, as stated before, $\phi_k(x)$ is a finite-support trilinear interpolating basis function, which means that for the estimation of the corresponding coefficient f_k, only the observation inside its region of support must be taken into account. The stopping criterion is the norm of the error $E = \|F^t - F^{t-1}\|$, which is the difference between two consecutive estimations.

IV. Characterization of Plaque Echo Morphology and Labeling

Characterization of plaque echo morphology is usually based on statistics computed from the observed noisy images. In this paper, the characterization is obtained from statistical estimators (15) depending on the continuous function $f(x)$ estimated in Section III-C. The scalar function $f(x) : R^3 \to R$ describes the Rayleigh parameters within the plaque volume that are related to the acoustic properties of the plaque components [24].

The proposed method is based on the automatic 3-D characterization of the plaque by use of 3-D US tools [9]. Visual assessment of carotid wall and plaque geometries as well as quantitative analysis of important clinical parameters, such as plaque volume, extension, maximum/mean stenosis, and its location along the plaque is provided automatically from the estimated meshes. Volume reconstruction of the plaque interior provides an overall characterization of its composition, which is, in most cases, mentally built up by the clinician.

Our method provides a computational tool for automatic characterization of plaque features, where the entire 3-D information is used. The local characterization of the plaque is based on the following statistical estimators for the mean $f_\mu(x)$, median (GSM) $f_\upsilon(x)$, standard deviation $f_\sigma(x)$, and percentile 40 $f_{P_{40}}(x)$ depending on $f(x)$ and derived from the Rayleigh distribution

$$\begin{cases} f_\mu(x) = \sqrt{\dfrac{\hat{f}(x)\pi}{2}} \\ f_\upsilon(x) = \sqrt{2\,\log(2)\hat{f}(x)} \\ f_\sigma(x) = \sqrt{\dfrac{4-\pi}{2}\hat{f}(x)} \\ f_{P_{40}}(x) = 1 - e^{[-(40^2)/2\hat{f}(x)]}. \end{cases} \tag{15}$$

Global measures of echogenicity and texture are computed by averaging the values of local estimators from the estimated continuous volume $\bar{f}_\tau = (1/V) \int_V f_\tau(x)\,dx$, where $\tau = \{\mu, \upsilon, \sigma, P_{40}\}$. These averaged values, however, despite their unquestionable usefulness, may not be enough for a correct assessment of plaque vulnerability, especially in cases where the plaque is significantly heterogeneous or is plagued by artifacts. In this paper, a local-based labeling approach was developed.

The goal is to use statistical estimators (15) to assess locally the risk of plaque rupture. Using this method, we expect to identify sites of the plaque whose features (hypoechogenicity and heterogeneity) point toward potential foci of vulnerability.

The classification of the plaque at each location x is made by comparison of the statistics for the mean, GSM, standard deviation, and P_{40} (15) with a threshold, defined by the clinician. This is done for every voxel, resulting in 3-D maps of labels ascribed for each one of the clinical indicators.

This thresholding algorithm is simple because it is performed on a voxel-by-voxel basis, without taking into account the neighboring nodes. Here, a more sophisticated and accurate method is used where the labeling procedure considers the intensity value of the statistical function at location x and also the values of its neighboring nodes. The goal is to introduce spatial correlation to reduce the misclassification rate by assuming that the plaque is composed of homogeneous regions separated by abrupt transitions. This assumption is acceptable from an anatomical perspective and is usually adopted in the denoising and deblurring of medical imaging.

Let f_k, as before, be the estimated value of $f(x)$ at the kth node. The labeled maps $\mathcal{L}_\tau$, with $\tau = \{\mu, \sigma, \upsilon, P_{40}\}$, are performed on a plane-by-plane basis, i.e., each plane is labeled independently of the others. The segmentation is binary, which means $\mathcal{L}(k) \in \{0, 1\}$, where $\mathcal{L}(k)$ is the kth node of the labeled volume. The labeling procedure of the whole volume is performed in three steps: 1) all stacked planes along the vertical direction are independently labeled; 2) all stacked planes along the horizontal direction are independently labeled; and 3) both volumes obtained in the previous steps, $\mathcal{L}_v(k)$ and $\mathcal{L}_h(k)$, are fused by making $\mathcal{L}(k) = \mathcal{L}_v(k) \otimes \mathcal{L}_h(k)$, where $\otimes$ denotes the Boolean product.

The labeling process of each plane is performed by solving the following optimization problem:

$$\mathcal{L}_\tau = \arg\min_{\mathcal{L}} E(F, \mathcal{L}) \tag{16}$$

where the energy function is

$$E(F, \mathcal{L}) = \sum_k (f_{\text{thrs}} - f_k)(2\mathcal{L}(k) - 1) + \alpha \sum_k \frac{[V(\mathcal{L}(k), \mathcal{L}(k_v)) + V(\mathcal{L}(k), \mathcal{L}(k_h))]}{\tilde{g}_k}. \tag{17}$$

In (17), $\mathcal{L}(k) \in \{0, 1\}$, α is a parameter to tune the strength of smoothness, f_{thrs} is the threshold, $\tilde{g}_k$ is the normalized ($\epsilon \leq \tilde{g}_k \leq 1$) gradient of $f(x)$ at the kth node, $\epsilon = 10^{-6}$ is a small number to avoid division by zero, and $\mathcal{L}(k_v)$ and $\mathcal{L}(k_h)$ are the labels of the causal vertical and horizontal neighbors of f_k. $V(l_1, l_2)$ is a penalization function defined as follows:

$$V(l_1, l_2) = \begin{cases} 0, & l_1 = l_2 \\ 1, & l_1 \neq l_2. \end{cases} \tag{18}$$

The energy function (17) is composed of two terms: the first called *data term* and the second called *regularization term*. The first forces the classification to be $\mathcal{L}(k) = 1$ when $f_k > f_{\text{thrs}}$ because this leads to a decrease in the term $(f_{\text{thrs}} - f_k)(2\mathcal{L}(k) - 1)$ when compared with the alternative solution, $\mathcal{L}(k) = 0$, and the reverse when $f_k < f_{\text{thrs}}$. The second term forces the uniformity of the solution because the cost associated with uniform labels is smaller than with nonuniform ones (18). In order to preserve the transitions, the terms are divided by the normalized gradient magnitude of $f(x)$, $\tilde{g}_k$. Therefore, when the gradient magnitude increases the regularization strength is reduced at that location.

The minimization of (17) formulated in (16) is a huge optimization task performed in the Ω^{NM} high-dimensional space, where $\Omega = \{0, 1\}$ is the set of labels, and N and M are the dimensions of the image. The optimal solution of the energy function (17) can be computed by using very fast and efficient algorithms based on graph cuts [25], [26]. For example, a 200×300 pixel image is processed in 0.2 s in an Intel Core 2 CPU at 1.83 GHz with 2 GB RAM, which shows the efficiency and the short processing time of the method.

V. Experimental Results

In this section, experimental results including the reconstruction of surfaces from real carotids and plaques are first shown. Then, the adequacy of 3-D reconstruction and characterization methods are assessed with synthetic data, and afterward, results using real medical data are presented.

A. Carotid and Plaque Surfaces

Surface reconstruction is displayed in a virtual reality modeling language (VRML) environment where it is possible to manipulate and magnify the 3-D models of carotids and plaques for better inspection of their morphologies. This allows us to evaluate the surface shape and extension of plaques and their precise location inside the carotid. Fig. 5(a) shows results of a normal carotid, where no plaque can be detected. On the other hand, Fig. 5(b) shows a diseased carotid, where a plaque is visible inside its structure. Fig. 5(c) depicts four plaques showing different sizes and shapes. On top, a real plaque is shown for comparison. Surface rendering allows a first-stage assessment of plaque risk in terms of extension, degree of stenosis, and surface morphology.

B. 3-D Echo Morphology

The performance of the reconstruction and labeling algorithms was evaluated with a "stack" of synthetically generated noiseless images of the plaque (Fig. 6). Not only is the algorithm able to attenuate the speckle noise, providing a clearer reconstructed volume than the original one, but it also allows us to identify the synthetically generated vulnerable regions across the plaque. Moreover, the true (noiseless) intensity values associated with these regions (GSM = 20) were correctly recovered.

A set of real data composed of $N = 60$ cross sections of a carotid artery of a patient with atherosclerosis (CN1A07) was used to illustrate the reconstruction procedure in more depth [Fig. 7(a)–(d)]. A regularization effect as well as attenuation of speckle noise is clearly observed from one image [Fig. 7(a)] to another [Fig. 7(c)]. This is also evident in observation of

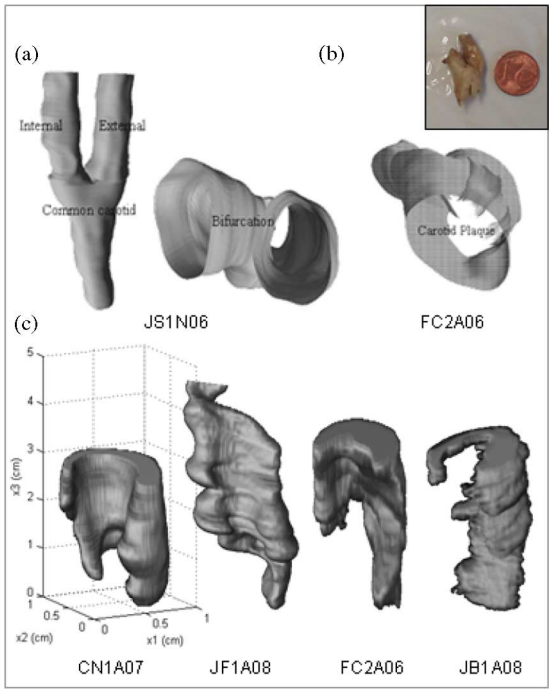

Fig. 5. (a) Surface rendering of normal carotids. (b) Surface rendering of diseased carotids. (c) Four plaques from different patients. (Top) Plaque after being surgically removed.

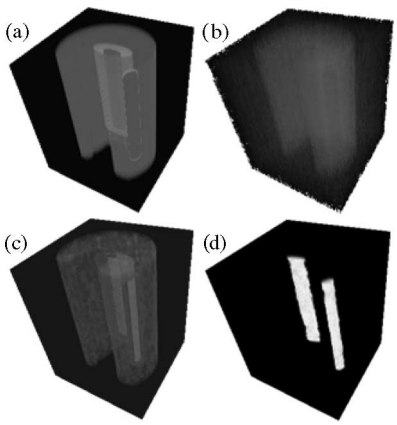

Fig. 6. (a) Reconstruction and labeling using a synthetic carotid plaque. Potentially vulnerable regions [two dark (GSM $= 20$) and one mid-gray (GSM $=$ 50)] were created. (b) Carotid plaque after being corrupted with Rayleigh noise. (c) Reconstructed plaque using the MAP method. (d) Vulnerable sites were correctly labeled (using GSM 32).

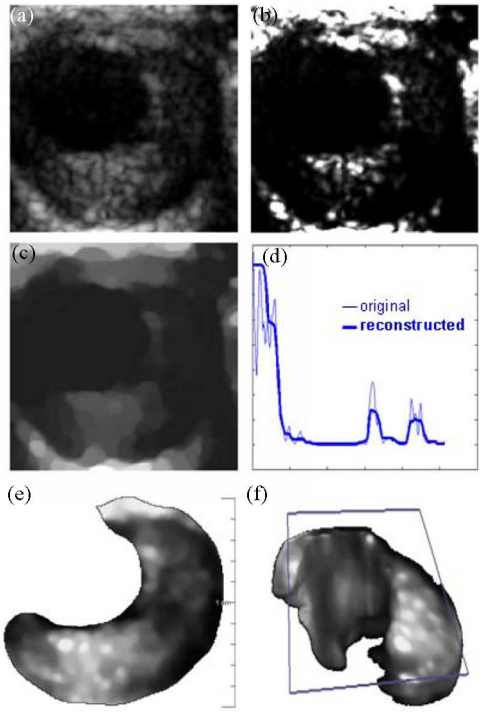

Fig. 7. Results of RF estimation and volume reconstruction. (a) Original of a cross section. (b) RF estimate of a cross section. (c) MAP estimate of a cross section. Grayscale intensity profile of the original and MAP estimate along a diagonal line. (e) Virtual cross section of the plaque, showing its grayscale composition. (f) Plaque morphology.

the profiles of both images along a diagonal line in Fig. 7(d). Fig. 7(e) displays a new generated cross section extracted from the estimated volume. This is a useful ability for better inspection of the morphology of the plaque without the presence of the patient. Using a region-growing algorithm, the plaque morphology is segmented and can easily be assessed, as shown in Fig. 7(f).

Table I shows a good agreement between the indicators determined by the clinician, using conventional 2-D methods, and those obtained automatically with the proposed 3-D method, namely the longitudinal extension of the plaque ℓ, mean μ, median υ, standard deviation σ, and P_{40}. Differences between the characterization using the conventional method and the proposed one are in almost all cases less than 10%. The similarity between the results of the two methods being compared is relevant because, from a clinical perspective, the medical information is considered to be the ground truth. The agreement between 2-D and 3-D results was expected because the plaques studied are quite homogeneous.

The analysis of plaque echo morphology, in particular, the GSM and the P_{40} (percentage of hypoechogenic voxels), determines whether (or not) the plaque is stable by using consensual thresholds given in literature, such as GSM < 32 and $P_{40} > 43$ [5]. This binary classification is, however, very simple and incomplete because it can lead to wrong diagnostic and clinical decisions. Furthermore, it does not give any information about the extension of unstable foci within the plaque.

The average parameter P_{40} obtained for all the studied plaques is greater than 50%, which means that more than half of their volumes present hypoechogenicity, but no information is given about the distribution of these sites throughout the plaques. Other important measures are the plaque volume and extension. Even more important is the study of the progression of these quantitative measures in time. This application is particularly suitable for this type of prospective clinical approach because it is much more accessible than other medical imaging modalities like CT and MRI.

Local characterization is clinically relevant for obtaining information about plaque local echo morphology that is not

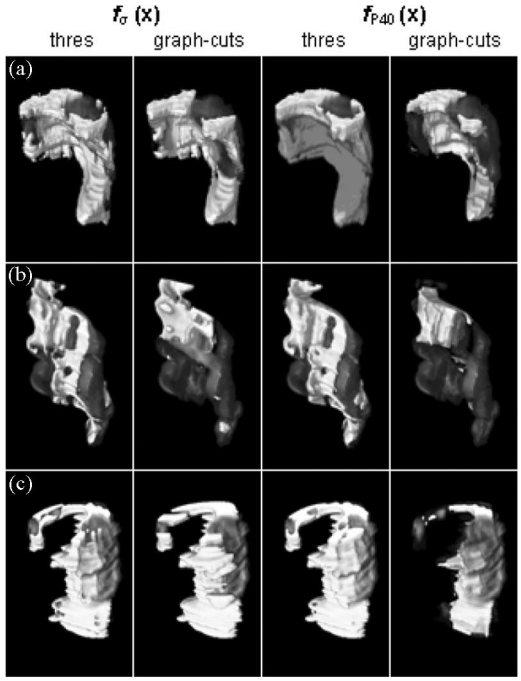

Fig. 8. Comparison of two labeling methods—thresholding and graph cuts—computed with the local Rayleigh estimators of median $f_\sigma(x)$ and P_{40} $f_{P40}(x)$ for three carotid plaques. (a) FC2A06. (b) JF1A08. (c) JB1A08.

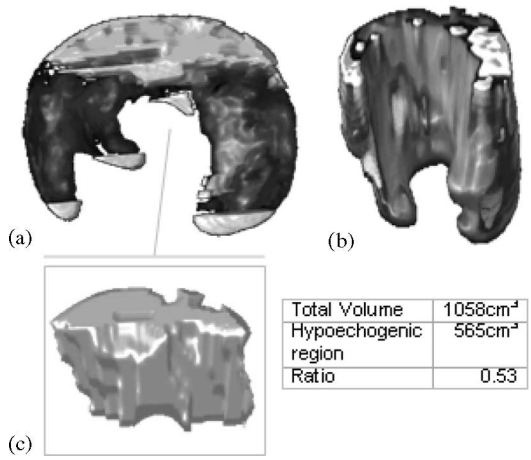

Fig. 9. Potential application of the algorithm. (a) Identification of hypoechogenic sites using the local median parameter. (b) Grayscale mapping of plaque texture using the local standard deviation parameter. (c) Inspection and quantification of a representative vulnerable region detected inside the plaque.

provided by global measurements. As previously described, this methodology is based on the computation of several statistical indicators, namely the mean, median, standard deviation, and P_{40} within the plaques.

Fig. 8 displays the labeling of potentially unstable sites across different plaques using two labeling methods: thresholding and graph cuts. It is observed that the labeling using graph cuts is less noisy and favors clustering, being more clinically meaningful than simple thresholding.

Another example is shown in Fig. 9. Here, regions of hypoechogenicity are identified by use of the local median estimator (GSM) [Fig. 9(a)]. Moreover, Fig. 9(b) shows results of plaque texture, based on the standard deviation [6], providing a grayscaled indicator of plaque heterogeneity. Regions resulting from the combination of the previous results are thought to be the most important foci of plaque rupture. Fig. 9(c) illustrates a potential application of the characterization algorithm based on the inspection of a region that was identified by the algorithm as being more vulnerable. This region can be extracted, its location inside the plaque can be tracked, and its volume can be computed to assess the ratio of its occupation related to the whole plaque.

VI. Conclusion

Plaque morphology and texture are considered to be powerful criteria to be added to the atherosclerosis diagnostic procedure. Two-dimensional ultrasound has so far been the preferred imaging technique because it is noninvasive, inexpensive, and widely used in most medical facilities.

The methodology proposed in this paper improves the characterization of carotid plaques by using a more accurate 3-D approach, together with new risk indicators and a local labeling of unstable foci within the plaque volume. Moreover, the acquisition protocol for plaque reconstruction does not need any equipment but the common scanner. This simplification leads to less accuracy than the one achieved with more complex techniques such as MRI. The proposed methodology, however, presents a novelty with respect to the traditional 2-D ultrasound methods while keeping the operating simplicity and accessibility. This framework allows a more complete and objective characterization than the traditional one because it considers all the information on carotid and plaque anatomies without depending on a subjective selection of a particular image for diagnosis.

Our approach allows a complete medical exam in less than 1 h, including image acquisition, reconstruction, segmentation, and classification. This performance is achieved because the segmentation is semiautomatic, which means that the carotid and plaque are usually segmented automatically without the need for medical intervention.

Results of the reconstruction and characterization were validated with synthetic data. Surface reconstruction was also validated by visual inspection made by an experimented clinician. Traditionally, the clinician makes a mental reconstruction and integration of the carotid and plaque anatomies. The results presented in this paper were validated on this basis by both qualitative opinion, according to the cutting planes used in reconstruction and representative longitudinal images (cross validation), and quantitative comparison with results obtained by using common 2-D analysis. In the future, comparison with results obtained with other medical imaging modalities, e.g., MRI, will be performed.

Furthermore, the method allows an accurate assessment of plaque composition on a local basis. This local characterization is crucial from a clinical perspective. The labeling procedure uses an efficient method based on graph cuts that allows us to identify sources of plaque rupture.

In summary, a 3-D ultrasound-based framework was introduced, which provides a complete and objective characterization of carotid plaques, with encouraging results in terms of plaque inspection, quantification, and both global and local characterization of echo morphology.

APPENDIX

POSITION ERRORS ANALYSIS

In this section, a displacement model for the ultrasound probe is derived and validated with real data acquired with an electromagnetic spatial locator (Fastrak, Pholemus, Colchester, VT). These data are used to characterize and quantify the errors between the true positions of the probe measured by the spatial locator and the estimated ones used by the algorithm.

The spatial locator provides three position and three orientation parameters of the sensor coupled to the probe. The distance between the transmitter (static referential) and the receptor (moving sensor) was kept small, less than 30 cm, to reduce measurement errors of the device (position accuracy of 0.08 cm rms).

Fig. 10(a) shows ten of these error signals computed as the difference between the real position measured by the spatial locator and the estimated one

$$e(n) = x(n) - \frac{x(N-1)-x(0)}{N}n - x(0), \quad 0 \le n \le N-1 \tag{19}$$

where $N = 400$, $x(0) = 0$, $x(N-1) = L$ with L corresponding to the distance between landmarks. Fig. 10(b) displays the mean of the absolute position error and orientation parameters computed over the 50 experimental sample signals. The averaged absolute error is less than 0.12 cm and the orientation angles are always constant to less than 1°. The standard deviation is also less than 1° for the orientation parameters and less than 0.25 cm for the position error.

Let the probe displacement be modeled as follows:

$$x(n) = x(n-1) + T\,v(n) \tag{20}$$

where T is the sampling period, $v(n) = v(n-1) + \eta(n)$, and $\eta(n)$ is a zero mean additive white Gaussian noise (AWGN).

The true and estimated positions, respectively, $x(n)$ and $y(n)$, are given by

$$x(n) = x(0) + nTv(0) + T\sum_{k=1}^{n}(n-k+1)\eta(k) \tag{21}$$

$$\begin{aligned} y(n) &= x(0) + \frac{x(N)-x(0)}{N}n \\ &= x(0) + nTv(0) + \frac{nT}{N}\sum_{k=1}^{N-1}(N-k+1)\eta(k) \end{aligned} \tag{22}$$

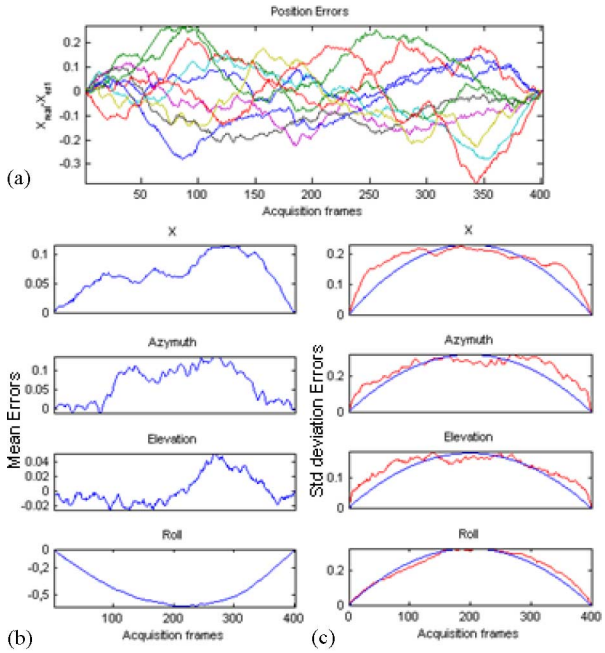

Fig. 10. (a) Experimental probe error signals computed as the difference between real and estimated positions. (b) Mean of position absolute errors and orientation parameters. (c) Standard deviation of errors in X, Azymuth, elevation, and roll.

where $v(0)$ is the initial velocity. Thus, the position error is

$$\begin{aligned} e(n) = x(n) - y(n) &= T\sum_{k=1}^{n}\left[\left(\frac{n}{N}-1\right)k - \left(\frac{n}{N}-1\right)\right]\eta(k) \\ &\quad - \frac{nT}{N}\sum_{k=n+1}^{N-1}(N-k+1)\eta(k). \end{aligned} \tag{23}$$

Assuming stationarity and independency for $\eta(n)$, its variance is

$$\sigma_e^2(n) = T^2\sigma_\eta^2 g(n) \tag{24}$$

where σ_η^2 is the unknown noise energy and

$$g(n) = \left(\frac{n}{N}-1\right)^2\sum_{k=1}^{n}(k-1)^2 + \left(\frac{n}{N}\right)^2\sum_{k=n+1}^{N-1}(N-k+1)^2. \tag{25}$$

The estimation of σ_η is obtained by use of the minimum square error (MSE) method from the observations

$$\hat{\sigma_\eta} = \arg\min_{\sigma_\eta}\sum_{n=0}^{N}\left[\sigma_{\exp}^2(n) - T^2\,g(n)\sigma_\eta^2\right]^2 \tag{26}$$

where $\sigma_{\exp}(n)$ is the experimental curve represented in Fig. 10(b), which was obtained by computation of the standard deviation over the 50 observations performed at the nth instant. The solution of (26) is

$$\hat{\sigma_\eta}^2 = \frac{1}{T^2}\frac{\sum_{n=0}^{N}\sigma_{\exp}^2}{g}(n)\sum_{n=0}^{N}g(n). \tag{27}$$

Let us now compute the relative measure of the standard deviation w.r.t. the average velocity. If the standard deviation of $\eta(n)$, $\sigma_\eta = p\bar{V}$, is a fraction of the average velocity, p may be estimated from the experimental data as follows:

$$\sigma_\eta = p\bar{V} \Rightarrow p \underbrace{\frac{\overbrace{x(N) - x(0)}^{L}}{NT}}_{\bar{V}} = \sigma_\eta \Rightarrow p = \frac{NT}{L}\sigma_\eta. \quad (28)$$

Typical values for N and L are 60 and 8 cm, respectively. The maximum standard deviation, occurring at the middle of the course [see Fig. 10(c)], which may be computed by (24), is $\sigma_e(N/2) = 0.17$ cm. The computation of p using (28) leads to $p = 0.01$, i.e., the velocity deviation estimated from the experimental data w.r.t. to its average value is only about 1% during the whole course. Therefore, it is concluded that the errors owing to variations on sweep velocity are small when compared with the total length of probe course.

It is observed that the standard deviation of the error is larger at the middle of the course and zero in its limits. This is an expected behavior, since we know its beginning, $x(1)$, and its ending, $x(N)$, so the major uncertainty is at the middle of the course. The theoretical curves, obtained from the model, are superimposed with experimental data and displayed in Fig. 10(c).

REFERENCES

[1] Consensus Group, "Consensus statement on the management of patients with asymptomatic atherosclerotic carotid bifurcation lesions: international angiology," *Int. Angiol.*, vol. 14, no. 1, pp. 5–17, 1995.

[2] H. Barnett, H. Meldrum, and M. Eliasziw, "The appropriate use of carotid endarterectomy," *Can. Med. Assoc.*, vol. 166, pp. 1169–1179, 2002.

[3] T. Elatrozy, A. Nicolaides, T. Tegos, and M. Griffin, "The objective characterization of ultrasonic carotid plaque features," *Eur. J. Vasc. Endovasc. Surg.*, vol. 16, pp. 223–230, 1998.

[4] R. Sztajzel, S. Momjian, I. Momjian-Mayor, N. Murith, and K. Djebaili, "Stratified gray-scale median analysis and color mapping of the carotid plaque: Correlation with endarterectomy specimen histology of 28 patients," *Stroke*, vol. 36, no. 4, pp. 741–745, 2005.

[5] L. Pedro, J. Fernandes, M. Pedro, and I. Gonçalves, N. Dias, "Ultrasonographic risk score of carotid plaques," *Eur. J. Vasc. Endovasc. Surg.*, vol. 24, pp. 492–498, Dec. 2002.

[6] L. Baroncini, A. Filho, L. Junior, A. Martins, and S. Ramos, "Ultrasonic tissue characterization of vulnerable carotid plaque: Correlation between videodensitometric method and histological examination," *Cardiovasc. Ultrasound*, vol. 4, p. 32, 2006, (Comparative study).

[7] A. Fenster, D. Downey, and H. Cardinal, "Three-dimensional ultrasound imaging," *Phys. Med. Biol.*, vol. 46, no. 5, pp. 67–99, May 2001.

[8] C. Ainsworth, C. Blake, A. Tamayo, V. Beletsky, and A. Fenster, "3D ultrasound measurement of change in carotid plaque volume: A tool for rapid evaluation of new therapies," *Stroke*, vol. 36, no. 9, pp. 1904–1909, 2005.

[9] U. Schminke, L. Motsch, L. Hilker, and C. Kessler, "Three-dimensional ultrasound observation of carotid artery plaque ulceration," *Stroke*, vol. 31, no. 7, pp. 1651–1655, 2000.

[10] J. Abbot and F. Thurstone, "Acoustic speckle: Theory and experimental analysis," *Ultrasound Imag.*, vol. 1, pp. 303–324, 1979.

[11] J. Sanches and J. Marques, "A multiscale algorithm for three-dimensional free-hand ultrasound," *Ultrasound Med. Biol.*, vol. 28, no. 8, pp. 1029–1040, 2002.

[12] V. Narayanan, P. Shankar, and J. Reid, "Non-Rayleigh statistics of ultrasonic backscattered signals," *IEEE Trans. Ultrason., Ferroelectr., Freq. Control*, vol. 41, no. 6, pp. 845–852, Nov. 1994.

[13] P. Shankar, "Ultrasonic tissue characterization using a generalized Nakagami model," *IEEE Trans. Ultrason., Ferroelectr., Freq. Control*, vol. 48, no. 6, pp. 1716–1720, Nov. 2001.

[14] J. Seabra and J. Sanches, "Modeling log-compressed ultrasound images for radio frequency signal recovery," in *Proc. Annu. Int. Conf. IEEE Eng. Med. Biol. Soc. (EMBC 2008)*, Vancouver, BC, Canada, pp. 426–429.

[15] K. Lekadir and G. Yang, "Carotid artery segmentation using an outlier immune 3D active shape model framework," in *Proc. MICCAI (1)*, 2006, pp. 620–627.

[16] C. M. van Bemmel, L. Spreeuwers, M. Viergever, and W. Niessen, "Level-set based carotid artery segmentation for stenosis grading," in *Proc. 5th Int. Conf. Med. Image Comput. Comput.-Assisted Intervention Conf.—Part II (MICCAI 2002)*. London, U.K.: Springer-Verlag, pp. 36–43.

[17] T. Eltoft, "Modeling the amplitude statistics of ultrasonic images," *IEEE Trans. Med. Imag.*, vol. 25, no. 2, pp. 229–240, Feb. 2006, (Comparative study).

[18] S. Gupta, L. Kaur, R. Chauhan, and S. Saxena, "A wavelet based statistical approach for speckle reduction in medical ultrasound images," *Med. Biol. Eng. Comput.*, vol. 42, no. 2, pp. 189–192, 2004.

[19] Z. Zeng and I. Cumming, "Bayesian speckle noise reduction using the discrete wavelet transform," in *Proc. Int. Geosci. Remote Sens. Symp.*, Jul. 1998, pp. 6–10.

[20] J. M. Sanches, J. C. Nascimento, and J. S. Marques, "Medical image noise reduction using the Sylvester–Lyapunov equation," *IEEE Trans. Image Process.*, vol. 17, no. 9, pp. 1522–1539, Sep. 2008.

[21] C. Xu and J. Prince, "Snakes, shapes, and gradient vector flow," *IEEE Trans. Image Process.*, vol. 7, no. 3, pp. 359–369, Mar. 1998.

[22] P. Besl and N. McKay, "A method for registration of 3-d shapes," *IEEE Trans. Pattern Anal. Mach. Intell.*, vol. 14, no. 2, pp. 239–256, Feb. 1992.

[23] J. Sanches, J. Dias, and J. Marques, "Minimum total variation in 3D ultrasound reconstruction," in *Proc. IEEE Int. Conf. Image Process. (ICIP 2005)*, Sep., vol. 3, pp. 597–600.

[24] C. Sehgal, "Quantitative relationship between tissue composition and scattering of ultrasound," *Acoust. Soc. Amer. J.*, vol. 94, pp. 1944–1952, 1993.

[25] Y. Boykov, O. Veksler, and R. Zabih, "Fast approximate energy minimization via graph cuts," *IEEE Trans. Pattern Anal. Mach. Intell.*, vol. 23, no. 11, pp. 1222–1239, Nov. 2001.

[26] V. Kolmogorov and R. Zabih, "What energy functions can be minimized via graph cuts?," *IEEE Trans. Pattern Anal. Mach. Intell.*, vol. 26, no. 2, pp. 147–159, Feb. 2004.

José C. R. Seabra (S'07) received the Diploma (M.Sc. degree) in biomedical engineering from the Technical University of Lisbon, Lisbon, Portugal, in 2007. He is currently working toward the Ph.D. degree in biomedical engineering from the Institute for Systems and Robotics, Instituto Superior Técnico, Lisbon.

Since 2006, he has been working in collaboration with the Cardiovascular Institute of Lisbon and Lisbon University Medical School. He is engaged in 3-D ultrasound-based techniques to monitor and characterize the carotid artery and atherosclerotic lesions. His current research interests include medical imaging, 3-D ultrasound, image processing, computer-aided diagnosis, and bioinstrumentation.

Dr. Seabra was awarded a Prize for the best graduation project in electrical and computer engineering, in 2007.

Luís M. Pedro received the M.D. and Ph.D.degrees.

He is a Consultant Vascular Surgeon and an Assistant Professor of vascular surgery at the Lisbon University Medical School, Hospital de Santa Maria, Lisbon, Portugal. His current research interests include noninvasive assessment of the arterial wall in atherosclerosis, ultrasonographic characterization of the atherosclerotic plaque, carotid surgery, and renovascular disease.

José Fernandes e Fernandes received the M.D. and Ph.D. degrees.

He is the Chief of Vascular Surgery, and the Chairman and a Full Professor of Surgery at the University of Lisbon Medical School, Hospital de Santa Maria, Lisbon, Portugal. His current research interests include vascular hemodynamics, noninvasive vascular evaluation, and morphological studies of arterial wall in atherosclerosis, vascular surgery, and endovascular reconstructions in both occlusive and aneurysmal disease.

João M. Sanches (M'05) received the Electr. Eng. and M.Sc. degrees, and the Ph.D. degree in medical imaging reconstruction from the Instituto Superior Técnico, Technical University of Lisbon, Lisbon, Portugal, in 1991, 1996, and 2003, respectively.

He is currently an Assistant Professor in the Electrical and Computer Engineering Department, Instituto Superior Técnico, Technical University of Lisbon, Lisbon, and where he is also a Researcher at the Institute for Systems and Robotics. He has taught in the area of signal processing and control. He is engaged in biomedical engineering, with several publications in this field. His current research interests include 3-D ultrasound, functional MRI, confocal imaging microscopy and neurophysiology.